

1 Gravity Inversion Method Using L_0 -norm Constraint
2 with Auto-adaptive Regularization and Combined
3 Stopping Criteria.

4 Mesay Geletu Gebre ^{1*} and Elias Lewi ²

¹Wolkite University, College of Natural and Computational Science,

P.O.Box 07, Wolkite, ETHIOPIA, E-mail: mesaygeletu@gmail.com

²Addis Ababa University, Institute of Geophysics, Space Science and Astronomy, Addis Ababa, ETHIOPIA

*Mesay Geletu, Email: mesaygeletu@gmail.com

Abstract

We present a gravity inversion method that can produce compact and sharp images, to assist the modeling of non-smooth geologic features. The proposed iterative inversion approach makes use of L_0 -norm stabilizing functional, hard and physical parameter inequality constraints, and depth weighting function. The method incorporates an auto-adaptive regularization technique, which automatically determines a suitable regularization parameter and error weighting function that helps to improve both the stability and convergence of the method. The auto-adaptive regularization and error weighting matrix are not dependent on the known noise level. Because of that, the method yields reasonable results even if the noise level of the data is not known properly. The utilization of an effectively combined stopping rule to terminate the inversion process is another improvement that is introduced in this work. The capacity and the efficiency of the new inversion method were tested by inverting randomly chosen synthetic and measured data. The synthetic test models consist of multiple causative blocky bodies, with different geometries and density distributions that are vertically and horizontally distributed adjacent to each other. Inversion results of the synthetic data show that the developed method can recover models that adequately match the real geometry, location, and densities of the synthetic causative bodies. Furthermore, the testing of the improved approach using published real gravity data confirmed the potential and practicality of the method in producing compact and sharp inverse images of the subsurface.

Keywords— Gravity data, Iterative inversion, L_0 -norm constraint, Auto-adaptive regularization, Stopping criteria, Compact image.

1 Introduction

Gravity measurements have been used in a wide range of geophysical prospecting and investigations, such as in mineral explorations, engineering and environmental problems as well as archeological site investigations (Hinze et al., 2013, p. 20). In general, gravity inversion is a process that is used to determine the density, size, shape, and location of complex subsurface causative bodies from an observed gravity anomaly, by using different mathematical modeling techniques. Thus, inversion of gravity data constitutes an important step in the quantitative interpretation since the reconstruction of density contrast models markedly increases the amount of information that can be extracted from the gravity data.

However, a principal difficulty with the gravity data inversion is the inherent non-uniqueness and instability that also exists in any geophysical method (Al-Chalabi, 1971; Blakely, 1996, p. 216). In other words, for the given observed gravity data there are many equivalent density distributions that can reproduce the same field data. The standard approach used to select acceptable solutions, that are geologically reasonable, is to use additional information about the problem by making assumptions on the following aspects: (1) about the model parameters (existing information on the subsurface structure from geological or other geophysical hindsight) and (2) about the data parameters (statistical properties of the inexact data, e.g. Gaussian distribution of errors). Based on these assumptions there are two approaches in gravity inversion: The first approach fixes the density and vary the geometry. This approach is nonlinear in nature and has been studied by many authors, for instance, Lelievre et al. (2015); Camacho et al. (2002) and Camacho et al. (2011). The second approach, which also is the one used in this work, fixes the geometry and vary the density. This approach is linear in nature and has been investigated by many researchers (Li and Oldenburg, 1998; Boulanger and Chouteau, 2001).

In an effort to introduce more qualitative prior information, Last and Kubik (1983) in particular, developed a method called compact gravity inversion. Their strategy utilizes the compactness stabilizer to minimize the area (in 2D) or volume (in 3D) occupied by the causative body, which is equivalent to maximizing its compactness. Barbosa and Silva (1994) generalized the compact inversion method by making use of compactness along several axes using Tikhonov's regularization. In 2006 Silva and Barbosa further developed the Compact inversion method with the so-called 'interactive inversion' which estimates the location and geometry of several density anomalies. They simplified their old method (Barbosa and Silva, 1994) to improve computational performance. The generalized compact and interactive inversion strongly need a priori information to yield an accurate estimation.

The compactness stabilizer (Last and Kubik, 1983) also known as the minimum support stabilizer (Port-

niaguine and Zhdanov, 1999) has been borrowed and implemented by other researchers in various geophysical inversion methods (Ajo-Franklin et al., 2007; Stocco et al., 2009; Fei et al., 2018; Feng et al., 2020; Varfinezhad et al., 2020). As it was demonstrated by a number of researchers (Zhdanov and Tolstaya, 2004; Rezaie et al., 2017; Feng et al., 2020; Varfinezhad et al., 2022), this stabilizer is known to yield a compact or focused geophysical model with sharp boundaries. Apart from the inversion methods which produce focused images mentioned above, sparse geophysical inversion approaches derived from L_p -norm ($0 \leq p \leq 1$) stabilization have been developed by many researchers. For instance, sparse seismic reflectivity inversion method (Li et al., 2017), direct current resistivity data inversion algorithm (Singh et al., 2018), magnetic data sparse inversion method (Li et al., 2018; Fournier et al., 2020), sparse gravity data inversion technique (Vatankhah et al., 2017; Peng and Liu, 2021), to mention only a few. Some instability of the original compact gravity inversion algorithm of Last and Kubik (1983) was reported by Lewi (1997, p. 87) when the data is contaminated with noise. Then Lewi (1997, p. 89) has improved the original compact inversion by introducing a new approach to the 3D compact gravity inversion. The problem with Lewi (1997, p. 89) method arises when dealing with a multiple-source model, where the inversion algorithm tends to concentrate densities towards the surface regardless of the true depth of the causative bodies. In overcoming this drawback, Gebre and Lewi (2022) improved the compact gravity inversion method by incorporating a new depth weighting function. In this paper, we present a gravity inversion method that can produce compact and sharp images, to assist the modeling of non-smooth, blocky geologic features with sharp boundaries. The proposed approach is based on the authors' previous work (Gebre and Lewi, 2022), to which the reader is referred for further details, with the following two main differences and advancements. The first is proposing and incorporating an auto-adaptive regularization and error weighting function. This has improved the fast convergence of the method while keeping its stability. The second is the implementation of combined stopping criteria to terminate the iteration after an appropriate number of steps. The developed method uses an iteratively reweighted least squares (IRLS) minimization algorithm in combination with L_0 -norm stabilizer, depth weighting and physical parameter inequality constraint to estimate a compact and sharp density contrast model of the subsurface.

86 2 Methodology

87 2.1 The 2D model

88 Most fixed geometry gravity inversion algorithms, including the one presented here, employ rectangular
 89 prismatic elements, to discretize the subsurface, owing to their flexibility in constructing complex
 90 models (Silva and Barbosa, 2006; Commer, 2011; Grandis and Dahrin, 2014). A 2-D model is obtained
 91 by discretization of the subsurface under the survey area into a large number of infinitely long horizontal
 92 rectangular prisms, with the infinitely long dimension oriented in the invariant y-direction, with
 93 variations in densities only assumed for the X and Z directions. The 2-D model is illustrated in Fig.
 94 1. The density contrasts are constant inside each cell only and can vary individually. Here we have
 95 used equal dimensions for the cells. However, the algorithm is flexible, to accommodate non-regular
 96 size cells. Gravity stations indicated by ∇ symbols are located at the centers of the upper faces of the
 97 rectangular blocks in the top layer. This discretization scheme of the subsurface allows us to calculate
 the gravitational attraction caused by each rectangular block separately.

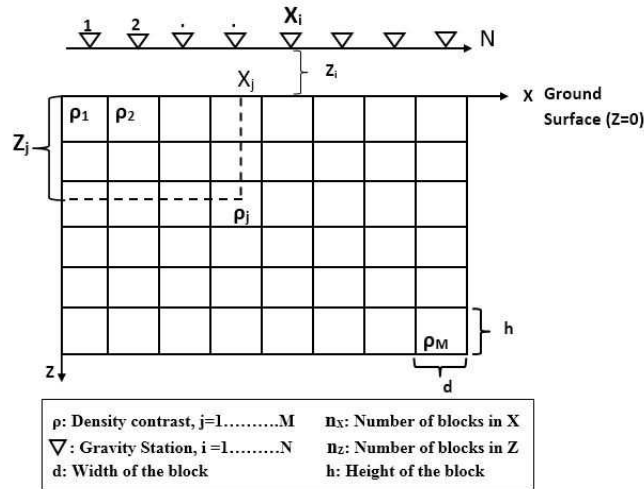


Figure 1: A 2-D model of the subsurface under a gravity profile. Gravity stations (X_i) are located at the centers of the blocks, indicated by the ∇ symbols.

98

99 2.2 Forward modelling

100 After discretization of the modeling space into a set of elementary rectangular blocks, the total vertical
 101 component gravity response calculated at the i^{th} observation point g_i is the sum of the gravity contribu-
 102 tions generated by each of the individual rectangular element, on all points belonging to the observation

103 grid and it is given by:

$$g_i = \sum_{j=1}^M a_{ij} \rho_j + e_i \quad i = 1, 2, 3, \dots, N \quad (1)$$

104 where ρ_j is the density of the j^{th} prism; N denotes the numbers of observations; a_{ij} is the contribution
105 of j^{th} prism to the gravity value on i^{th} observation point and e_i is the noise associated with i^{th} data point.
106 The kernel a_{ij} is the forward operator that maps from the physical parameter space to the data space.
107 The exact mathematical expression of the kernel used here is presented by Last and Kubik (1983) which
108 is adopted from Nagy (1966) to which the reader is referred for more detail mathematical development.
109 In matrix notation Eq. (1) can be written as:

$$\mathbf{g} = \mathbf{A}\boldsymbol{\rho} + \mathbf{e} \quad (2)$$

110 where \mathbf{g} is an N-dimensional vector containing the gravity values, $\boldsymbol{\rho}$ is an M-dimensional model vector
111 of densities, \mathbf{A} is the N x M kernel matrix, and \mathbf{e} represents the noise vector at data points. Equation
112 (2) constitutes the gravity forward modeling, i.e. used to calculate the predicted gravity anomalies
113 (theoretical data) for a known subsurface density contrast (model $\boldsymbol{\rho}$).

114 **2.3 Inverse Modeling**

115 Our objective in solving gravity inverse problems is given the observed gravity data (\mathbf{g}), we seek a
116 solution that gives a density distribution $\boldsymbol{\rho}$ which predicts the observed data with a certain noise level
117 and at the same time, satisfies certain constraints. For the model presented here, the density vector
118 $\boldsymbol{\rho}$ is related to the predicted gravimetric field \mathbf{g} by the linear expression given in Eq. (2). Like the
119 majority of practical inverse problems arising in geophysical modeling gravity inversion is an ill-posed
120 problem. Moreover, usually we have less number of the observed gravity data than the number of the
121 model parameters which makes the system an under-determined problem. A standard way to solve such
122 ill-posed and under-determined problems, according to regularization theory (Tikhonov et al., 2013), is
123 minimization of the following objective function (Φ) which is the combination of data fidelity or misfit
124 functional (Φ_d) and stabilizing functional (stabilizer) term ($S(\rho)$):

$$\Phi = \Phi_d + \ell^2 S(\rho) \quad (3)$$

125 Here the misfit functional is $\Phi_d = \|\mathbf{W}_e(\mathbf{A}\boldsymbol{\rho} - \mathbf{g}^{obs})\|_2^2$ and \mathbf{W}_e is error weighting diagonal matrix.
126 In Eq. (3), ℓ is a regularization parameter that controls the trade-off between the data fidelity and the
127 stabilizing term. Choosing a small value improves the data fit but the recovered models have highly
128 oscillatory artificial structures (which is equivalent to under-regularization). On the other hand, a large
129 value of ℓ leads to a large misfit value between the observed and predicted data and a small norm of the
130 model (over-regularizing the solution). Thus, the choice of a suitable value for ℓ is very important.
131 The choice of the stabilizing functional, in Eq. (3), depends on the desired model features that are to
132 be recovered. There are several types of stabilizers that have been developed and implemented in the
133 inversion of potential field data, which can roughly be divided into two categories: (I) Smooth stabilizer
134 which uses L_2 -norm of the model parameters or gradient of the model parameters (Li and Oldenburg,
135 1998; Cella and Fedi, 2012; Paoletti et al., 2013). (II) Non-smooth stabilizer which uses L_1 -norm or
136 L_0 -norm directly on the model parameters or on the gradient of the model parameters (Bertete-Aguirre
137 et al., 2002; Sun and Li, 2014; Li et al., 2018; Utsugi, 2019). Inversion methods that utilize a smooth
138 stabilizer produce model typically characterized by smooth features, and hence have difficulties in re-
139 covering blocky structures or non-smooth distributions that have sharp boundaries or abrupt changes in
140 physical properties (Farquharson, 2008). To overcome this problem, non-smooth stabilizers that help to
141 produce compact and sharp models have been applied successfully (Zhdanov, 2009; Meng et al., 2018).
142 Since we are interested in developing a gravity inversion method that can produce compact and sharp
143 models, we use a non-smooth stabilizer through the L_0 -norm on the model parameters and will be dis-
144 cussed in the next subsection. In general, with all mentioned stabilizers Eq. (3) needs to be solved
145 by using an iterative minimization algorithm. In this work, we use the IRLS algorithm to estimate the
146 solution and it is described below.

147 Using the classical weighted L_2 -norm stabilizing functional $S(\boldsymbol{\rho}) = \|\mathbf{W}_c(\boldsymbol{\rho} - \boldsymbol{\rho}_F)\|_2^2$ in the objective
148 function Φ (Eq. (3)) and minimizing by applying the standard weighted-damped least-square optimiza-
149 tion, the estimated density distribution in matrix notation can be given by (Menke, 1989, p. 55):

$$150 \quad \boldsymbol{\rho}^{k+1} = \boldsymbol{\rho}_F^k + \left[[\mathbf{W}_c^k]^{-1} \mathbf{A}^T \left(\mathbf{A} [\mathbf{W}_c^k]^{-1} \mathbf{A}^T + \ell^2 [\mathbf{W}_e^k]^{-1} \right)^{-1} \mathbf{g}_r^k \right] \quad (4)$$

151 where the superscript k denotes that variable at k^{th} iteration and \mathbf{W}_c^k is a combined weighting matrix.
152 $\boldsymbol{\rho}_F^k$ is reference density vector, which is from prior information or calculated at each iteration. $\mathbf{g}_r^k =$
153 $\mathbf{g}^{obs} - \mathbf{A}\boldsymbol{\rho}_F^k$ represents residual data vector computed at each iteration. Computation of the regularization

154 parameter ℓ in Eq. (4) will be described in Sect. 2.3.3. In this work, the combined weighting matrix
 155 (\mathbf{W}_c^k) is defined as a product of three different diagonal matrices, L₀-norm constraint matrix ($\mathbf{W}_{L_0}^k$),
 156 depth weighting (\mathbf{W}_z) and hard constraint matrix (\mathbf{W}_h^k).

$$\mathbf{W}_c^k = \mathbf{W}_{L_0}^k \mathbf{W}_z \mathbf{W}_h^k \quad (5)$$

157 2.3.1 L₀-norm Constraint

158 The L₀-norm is commonly defined as the number of nonzero elements in a vector. Because there is no
 159 analytical formula that meets the mathematical requirement to be regarded as L₀-norm, the approximate
 160 expression is usually used to convert the L₀-norm into an equivalent norm for the suitability of computa-
 161 tion. In literature (Zhao et al., 2016; Li and Yao, 2020) that discusses the inversion of potential field data,
 162 different L₀-norm approximate stabilization functions have been developed and implemented to obtain
 163 focused images and sharp boundaries. Meng (2016) used a hyperbolic tangent function to approximate
 164 the L₀-norm and applied it to the 3D inversion of gravity gradient tensor data. Meng et al. (2018) pro-
 165 posed an exponential mathematical function to approximate the L₀-norm for 3D gravity sparse inversion.
 166 In this paper, the minimum support functional, which is also called compactness constraint originally
 167 proposed by Last and Kubik (1983) and then further extended by Portniaguine and Zhdanov (1999) to
 168 include a reference model is selected which can be expressed as follows:

$$L_0(\rho) = \sum_{j=1}^M \frac{(\rho_j - \rho_j^{apr})^2}{(\rho_j - \rho_j^{apr})^2 + \varepsilon} \quad (6)$$

169 In our case to avoid the requirement of a prior model, we set $\rho_j^{apr} = 0$ and hence Eq. (6) can be rewritten
 170 as follows (Sun and Li, 2014):

$$L_0(\rho) = \sum_{j=1}^M \frac{\rho_j^2}{\rho_j^2 + \varepsilon} \quad (7)$$

171 where ε is a focusing parameter. Application of $L_0(\rho)$ as stabilizer in minimization process of the
 172 objective function (Eq. (3)) leads to the following choice of an L₀-norm constraint matrix \mathbf{W}_{L_0} which is
 173 given by (Last and Kubik, 1983):

$$[\mathbf{W}_{L_0}]_j = ([\rho_j]^2 + \varepsilon)^{-1} \quad (8)$$

174 Based on Eq. (8) the k^{th} iteration diagonal elements of the L_0 -norm constraint matrix ($\mathbf{W}_{L_0}^k$) can be
 175 formulated as follows:

$$[\mathbf{W}_{L_0}^k]_{jj}^{-1} = [\rho_j^{k-1}]^2 + \varepsilon \quad (9)$$

176 The focusing parameter ε is a very important parameter. Its main purpose is to avoid singularities when
 177 $\rho_j \rightarrow 0$. The parameter ε is a small number and in general, we are interested in the case where $\varepsilon \rightarrow 0$
 178 because a small value leads to very compact models. However, this may introduce instability. On the
 179 other hand, if ε is chosen large the L_0 -norm compactness constraint has no influence on the compactness
 180 of the model which means it results in a smooth solution. Figure 2 shows the comparison of the minimum
 181 support stabilizing functional for different values of ε to demonstrate the impact of the choice of different
 182 values of ε further. From Fig. 2, one can see that as ε becomes large the minimum support stabilizing
 183 function loses its property and behaves more like the minimum length L_2 -norm stabilizer which results
 184 in undesirable smoothness in the model though it improves the stability. Therefore, it is essential to
 choose an optimal value of ε .

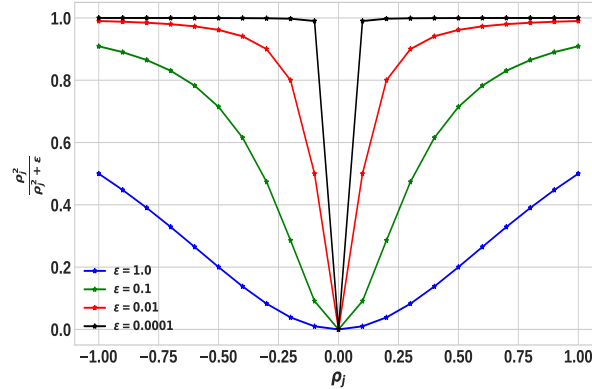


Figure 2: Comparison of the minimum support stabilizing function for different values of ε .

185

186 In previous investigations e.g Last and Kubik (1983) and Guillen and Menichetti (1984) the parameter
 187 ε was assigned a value close to machine precision ($\approx 10^{-11}$ to 10^{-15}). Alternatively, Zhdanov and
 188 Tolstaya (2004) introduced a trade-off curve method, similar to the L-curve technique, to select ε by
 189 computing the model objective for the current model estimate over a range of values for ε . However,
 190 as pointed out by Ajo-Franklin et al. (2007) setting ε to values near machine precision results in severe
 191 instability as $\rho_j \rightarrow 0$ and the approach of Zhdanov and Tolstaya (2004) often yields trade-off curves
 192 with corners that are not well defined. Therefore it is better to fix ε at a reasonable value determined by
 193 experience, typically between 10^{-4} to 10^{-7} (Ajo-Franklin et al., 2007). Accordingly, in the present

194 work based on several numerical simulation tests, the value 10^{-6} is assigned just for the inversion
 195 examples presented in the manuscript. Note that the developed method is flexible to use different values
 196 of ε .

197 2.3.2 Error weighting

198 According to compact inversion method proposed by Last and Kubik (1983), the k^{th} iteration error
 199 weighting matrix \mathbf{W}_e^k is defined as:

$$[\mathbf{W}_e^k]^{-1} = \text{diag} \left(\mathbf{A} [\mathbf{W}_{L_0}^k]^{-1} \mathbf{A}^T \right) \quad (10)$$

200 Even though \mathbf{W}_e^k expressed by Eq. (10) is applied by many authors (Guillen and Menichetti, 1984;
 201 Barbosa and Silva, 1994; Ghalehnoee et al., 2017; Gebre and Lewi, 2022), some instability was reported
 202 by Lewi (1997, p. 87) in using \mathbf{W}_e^k in scenarios such as complicated geological geometry and when the
 203 data is contaminated with noise. To overcome this problem Lewi (1997, p. 90) proposed a weighting
 204 matrix that makes use of the following equation:

$$[\mathbf{W}_e^k]^{-1} = \left[\frac{[\sigma_\rho^2]^k}{1 + [\sigma_e^2]^k} \right] \mathbf{I} \quad (11)$$

205 where \mathbf{I} represents identity matrix, and σ_ρ^2 and σ_e^2 are model and error variances respectively that are
 206 given by:

$$[\sigma_e^2]^k = \frac{\sum_{i=1}^N \{ \mathbf{g}_i - \sum_{j=1}^M a_{ij} [\boldsymbol{\rho}_j^{k-1}] \}^2}{N - 1} \quad (12)$$

208

209

$$[\sigma_\rho^2]^k = \frac{\sum_{j=1}^M [\boldsymbol{\rho}_j^{k-1}]^2}{M - 1} \quad (13)$$

210 The term in square brackets in Eq. (11) can be considered as regularization parameter (Silva and Bar-
 211 bosa, 2006; Lewi, 1997, p. 90). Based on several numerical experiments done in the present work it was
 212 observed that this term can sometimes ends up in a larger value which may result in over-regularization
 213 of the solution. For this reason, in the present study, a new error weighting matrix \mathbf{W}_{ne}^k is introduced
 214 and it is given as:

215

$$[\mathbf{W}_{ne}^k]^{-1} = \text{diag} \left(\mathbf{A} \left[\mathbf{W}_z \left(\frac{[\sigma_\rho^2]^k}{1 + [\sigma_e^2]^k} \right) \mathbf{W}_h^k \right] \mathbf{A}^T \right) \quad (14)$$

216 Let us represent the terms in square brackets by \mathbf{W}_n^k as follows:

$$217 \quad \mathbf{W}_n^k = \mathbf{W}_z \left(\frac{[\sigma_\rho^2]^k}{1 + [\sigma_e^2]^k} \right) \mathbf{W}_h^k \quad (15)$$

218 where \mathbf{W}_z and \mathbf{W}_h^k are diagonal depth and hard constraint matrices respectively and will be described in
 219 the next subsections. Then the error weighting matrix in Eq. (14), the one introduced and implemented
 220 here becomes:

$$[\mathbf{W}_{ne}^k]^{-1} = \text{diag} \left(\mathbf{A} \mathbf{W}_n^k \mathbf{A}^T \right) \quad (16)$$

221 **2.3.3 Auto-adaptive Regularization Parameter Estimation**

222 Choosing a suitable value for the regularization parameter is a crucial part of the inversion process. The
 223 precise value of the regularization parameter depends on the noise level associated with the observed
 224 data. Thus, the higher value of ℓ refers to the higher noise level of the data points. Several methods
 225 have been proposed to choose the appropriate value of regularization parameter, and are reviewed in the
 226 literature (Farquharson and Oldenburg, 2004; Vatankhah et al., 2014) and standard texts for example
 227 Vogel (2002, pp. 97-109) and Aster et al. (2018, p. 57). Particularly, depending on the noise level
 228 a constant value of ℓ , throughout the inversion, has been chosen by many authors (Silva and Barbosa,
 229 2006; Ghalehnoee et al., 2017). In other works, for example Zhdanov (2009) and Rezaie et al. (2017)
 230 the parameter ℓ has been iteratively updated in each iteration.

231 As pointed out in previous works (Farquharson and Oldenburg, 2004; Gholami and Aghamiry, 2017)
 232 instead of using a constant value of ℓ , dynamic re-adjustment throughout the iterative scheme might be
 233 a superior approach. Taking this into account, in the present work ℓ is updated in each iterative step.
 234 In our implementation, to select an optimal regularization parameter at each iteration, we proposed an
 235 auto-adaptive regularization method. This method leads to an automatic update of the regularization
 236 parameter at each and every iteration. The basic principle including its procedure in relation to the
 237 formally known adaptive regularization approach which was proposed by Zhdanov (2002, p. 55) and
 238 implemented by many authors (Zhdanov, 2009; Rezaie et al., 2017) is as follows. In adaptive regular-
 239 ization approach the initial value of the regularization parameter ℓ^1 is updated at each iteration step by
 240 (Zhdanov, 2002, p. 55):

$$\ell^k = \ell^1 q^k \quad (17)$$

241 where q , as described by Zhdanov (2002, p. 55), is damping factor which decreases from iteration to
 242 iteration. Its initial value is empirically determined having a value between zero and one. It is obvious
 243 that the trial and error selection of the value for q requires computational work . The presented auto-
 244 adaptive regularization method overcomes this problem and the iterative values ℓ^k are determined by the
 245 following formula:

$$\ell^k = \ell^{k-1} \left[\frac{|g^{obs} - A\rho|_{max}^{k-1}}{|g^{obs} - A\rho|_{max}^k} \right] \quad (18)$$

246 where the term in the square bracket is an adjusting factor that is automatically determined at each
 247 iterative step and $|g^{obs} - A\rho|_{max}$ is the maximum absolute value of the residual data elements. In
 248 the auto-adaptive regularization method, choosing a suitable initial value of (ℓ_o) is essential. Based
 249 on a number of synthetic and real data simulations done in this work we recommend the following in
 250 choosing a reasonable value of ℓ_o : Firstly, the initial value of ℓ should be within the range $0 < \ell_o \leq 1$.
 251 Secondly, the precise value of ℓ_o depends on the noise level related to the observed data. When the
 252 probable or expected noise level of the data is higher, a larger value ℓ_o is a reasonable choice to avoid
 253 unwanted and false anomalies due to noise. In contrast, when the probable or expected noise level is less
 254 a small value of ℓ_o should be chosen. Once an appropriate initial value ℓ_o is given as an input, then for
 255 subsequent iterations Eq. (18) is used to determine ℓ^k . The advantage of the auto-adaptive regularization
 256 scheme is its capability to automatically determine a suitable regularization parameter, in the course of
 257 the optimization process, depending on the automatically determined adjusting factor.

258 **2.3.4 Physical Parameter Inequality Constraint**

259 To produce a physically meaningful model from a gravity inverse solution, the usage of lower and
 260 upper bound constraints on the recovered density contrast is beneficial (Silva et al., 2001; Grandis and
 261 Dahrin, 2014). Lower and upper bounds can be obtained from a prior information such as geological
 262 investigations in conjunction with published density values of rocks, well-logging, and/or laboratory
 263 tests. Many procedures such as gradient projection approach (Wang and Ma, 2007; Lelièvre et al., 2009),
 264 transform function approach (Pilkington, 2008) and logarithmic barrier approach (Li and Oldenburg,
 265 2003) have been applied in different inversion schemes to implement this constraint. However, with
 266 regard to L_0 -norm stabilizer based gravity inversion methods an effective method is the direct utilization
 267 of lower and upper density constraints (Meng et al., 2018). Hence, in this work the direct density
 268 bound inequality constraint is used, that is at each iteration density contrast of each rectangular block is

269 bounded by minimum and maximum density constraint function given by:

$$270 \quad [\rho^k]_j = \begin{cases} [\rho_{max}]_j & \text{if } [\rho^k]_j > [\rho_{max}]_j \\ [\rho^k]_j & \text{if } [\rho_{min}]_j < [\rho^k]_j < [\rho_{max}]_j \\ [\rho_{min}]_j & \text{if } [\rho^k]_j < [\rho_{min}]_j \end{cases} \quad (19)$$

271 By using this function, if k^{th} iteration ρ_j of any block exceeds one of its bounds, then it will be fixed at
272 the violated bound.

273 In each iteration step the procedure to compute the hard constraint matrix \mathbf{W}_h^k (Boulangier and Chouteau,
274 2001) and the reference density vector ρ_F^k is determined as follows: The diagonal elements of \mathbf{W}_h^k are
275 fixed at ε or 1.0. When a prior geological and geophysical information are able to provide the initial
276 value of density contrast of the j^{th} specific cells, then these values are assigned to the corresponding
277 $[\rho_F^k]_j$. Simultaneously, the corresponding diagonal elements of $[\mathbf{W}_h^k]_{jj}$ are set to be ε . During the in-
278 version process, if the j^{th} elements of estimated density values falls out of inequality constraint limits
279 defined by ρ_{min} and ρ_{max} , then $[\rho_F^k]_j$ will be fixed at the violated bound density itself and $[\mathbf{W}_h^k]_{jj}$
280 assigned to be ε . On the other hand, if the elements of the estimated density did not exceed its bounds
281 (i.e. lies between the limits), $[\mathbf{W}_h^k]_{jj}$ and $[\rho_F^k]_j$ are assigned to be 1.0 and 0.0 respectively.

282 Using \mathbf{W}_h^k any blocks whose density is known from a priori information or exceeds the density con-
283 straint limit, the algorithm will automatically freezes this block in the next iteration by assigning a very
284 small weight to it. Whereas, ρ_F^k is used to remove the gravity effects of those cells that have crossed
285 the inequality constraint limit from the observed gravity data. That is applied to compute the reduced
286 gravity data vector $\mathbf{g}_r^k = \mathbf{g}^{obs} - \mathbf{A}\rho_F^k$ in Eq. (4) of the inversion algorithm. In other word, at each
287 iterative step the inversion of subsequent iteration will be performed using reduced gravity data vector.

288 2.3.5 Depth weighting

289 It is well known that gravity data, like any potential field data, has no inherent depth resolution. The
290 reconstructed model structures by the inversion process tend to concentrate near the surface regardless
291 of the true depth of the causative bodies (Li and Oldenburg, 1996). This happens because the inverse
292 solution of model construction is a linear combination of kernel, whose amplitudes rapidly decay with
293 depth. The problem can be overcome by introducing a depth weighting matrix to counteract the natural
294 decay of kernel with depth (Li and Oldenburg, 1998). Depth weighting is designed to ensure that all
295 cells have equal likelihood to accommodate the sources, not just those at shallow levels that are most

296 sensitive to the observed data. Depth weighting is used and its effect is investigated by different authors
 297 (Pilkington, 2008; Commer, 2011). Based on Gebre and Lewi (2022), the recently proposed depth
 298 weighting function is given as follows:

$$299 \quad w_{zj} = (aZ_j + c_o)^{-\tau} \quad (20)$$

300 where Z_j is the mean depth of the j^{th} cell and a , c_o and τ are adjustable parameters. The values of
 301 the three adjustable parameters are computed by optimizing $w_z(z)$ to match with the actual gravity
 302 kernel values utilizing nonlinear least-squares minimization (Virtanen et al., 2020). Accordingly, for all
 303 inversions in this work the depth weighting matrix similar to the one used by Gebre and Lewi (2022) is
 304 employed (Eq. (21)):

$$305 \quad [\mathbf{W}_z]_{jj} = \mathbf{diag}(w_{zj}) \quad (21)$$

306 where \mathbf{W}_z is diagonal M x M depth weighting matrix.

307 2.3.6 Stopping Criteria

308 It is clear that if the iterations are stopped too early, then a reasonable solution of the inverse problem may
 309 not be obtained. On the other hand, too many iterations may waste computer time without increasing the
 310 overall solution qualities. Thus, an important aspect of any iterative inversion method is to decide when
 311 the iterations should be terminated. A number of stopping criteria have been proposed and employed
 312 to terminate iterative inversion algorithms (Borges et al., 2015; Levin and Meltzer, 2017). Commonly
 313 used stopping criteria are based on a norm of the residual vector (i.e. the norm of the difference between
 314 estimated and observed data). For instance, a noise level, i.e. $\chi^2 = \|\mathbf{W}_d(\mathbf{g}^{obs} - \mathbf{A}\boldsymbol{\rho})\|_2^2$, where a
 315 diagonal data weighting matrix \mathbf{W}_d , whose i^{th} element is the inverse of the standard deviation of the
 316 noise at each data point, is used by Boulanger and Chouteau (2001) and Vatankhah et al. (2017). Other
 317 criteria for stopping gravity inversion procedure are based on simple *misfit* or the Root Mean Square
 318 Error (*RMSE*) between the observed data and predicted data produced by the recovered model (see, for
 319 example Rezaie and Moazam (2017)). The expressions used to estimate these criteria are the following:

$$320 \quad misfit = \left(\frac{\sum_{i=1}^N (\mathbf{g}_i^{obs} - \mathbf{g}_i^{cal})^2}{\sum_{i=1}^N (\mathbf{g}_i^{obs})^2} \right)^{\frac{1}{2}} \quad (22)$$

$$321 \quad RMSE = \frac{(\sum_{i=1}^N (\mathbf{g}_i^{obs} - \mathbf{g}_i^{cal})^2)^{\frac{1}{2}}}{N} \quad (23)$$

323 Ekinci (2008) also introduced other possible criterion, namely the parameter variation function (*smv*)
 324 which is defined as:

$$325 \quad smv = \left(\sum_{j=1}^M (\rho_j^k - \rho_j^{k-1})^2 \right)^{\frac{1}{2}} \quad (24)$$

326

327 The most widely used approach is to quit the iterative process when one of the above criteria are below
 328 a given tolerance (the level of observational error). However, in practical applications a precise value
 329 for such tolerance is rarely known; rather, only some possibly vague idea of the desired quality of
 330 the numerical approximation is at hand. Moreover, it has been pointed out by Rao et al. (2018) that
 331 stopping iteration based solely on the norm of the residual is neither safe nor a robust solution. The
 332 non-uniqueness and instability of the gravity inverse problem further complicates the usage of only
 333 one of the aforementioned stopping criteria. To overcome these issues, a combination of the *misfit*
 334 and *smv* has been utilized in this paper. Therefore, the iterative procedure continues until one of the
 335 following stopping criteria is met: (I) the maximum number of iteration (k_{max}) given by the user is
 336 reached or (II) the difference between two consecutive iteration values of *smv* and *misfit* have reached
 337 the target values. That means for the second criterion both the conditions $|smv^{k-1} - smv^k| \leq \tau$ and
 338 $|misfit^{k-1} - misfit^k| \leq \mu$ must be satisfied at the same time. In all demonstrations considered in this
 339 work, after testing different values, the parameter τ is assigned to $\sqrt{2M}$; and μ to 0.005. Where M is
 340 again the total number of model parameters. The effectiveness of the proposed termination criteria will
 341 be illustrated by using synthetic tests.

342 **2.4 Computational procedure**

343 The solution of the linear system of equations in Eq. (2) will be carried iteratively using the information
 344 about the misfit and density from successive iteration. The input parameters for the inversion proce-
 345 dure are: (1) Kernel matrix (\mathbf{A}) and discretized subsurface model (mesh) and its initial approximation
 346 reference density model ρ_F if exists based on a priori information; (2) Observed gravity anomaly (\mathbf{g})
 347 at measurement points (\mathbf{x}); (3) Maximum number of iteration (k_{max}) and the constant β ; (4) Lower
 348 ρ_{min} and upper ρ_{max} density bounds and initial ℓ_o value. In summary, the steps taken to carry out the
 349 inversion process consists the followings.

- 350 1. For $k = 0$, if there is no a priori information, \mathbf{W}_{L_0} , \mathbf{W}_c , \mathbf{W}_n and \mathbf{W}_h are identity matrices,
 351 $\rho_F = 0$. \mathbf{W}_z and \mathbf{W}_{ne} are computed through Eq. (21) and (16) respectively, after this, the first

- 352 iteration model parameters solution is obtained by Eq. (4).
- 353 2. The elements of \mathbf{W}_h and ρ_F are updated as explained in preceding section, then \mathbf{W}_{L_0} is calcu-
354 lated using Eq. (9) and then \mathbf{W}_c using Eq. (5).
- 355 3. Compute the value of σ_ρ and σ_e using expressions (13) and (12) respectively. Then calculate \mathbf{W}_n
356 using Eq. (15).
- 357 4. To remove the effect of those blocks that have crossed the maximum target density, evaluate the
358 reduced data $\mathbf{g}_r^k = \mathbf{g}^{obs} - \mathbf{A}\rho_F^k$. Then compute the current ℓ with Eq. (18) and \mathbf{W}_{ne} with Eq.
359 (16).
- 360 5. Carrying out the inversion through Eq. (4).
- 361 6. Application of bounded constraints on density are carried out as discussed in the preceding sec-
362 tion.
- 363 7. Now a forward modelling procedure will be carried out using Eq. (2) to compute the gravity
364 anomaly \mathbf{g}^{cal} from the estimated model in the previous iteration.
- 365 8. Data *misfit* (Eq. (22)) and *smv* (Eq. (24)) are computed using \mathbf{g}^{cal} from step 7, and obtained
366 model parameters from the previous and current iteration.
- 367 9. Test if the stopping criteria are fulfilled. If the termination criteria are satisfied the iteration
368 terminates and obtained results are stored and plotted. Otherwise, using the current estimated
369 density model, move to the next iteration k by going to the second step and continue the iterative
370 procedure until the stopping criteria are fulfilled.

371 **3 Synthetic Model Test**

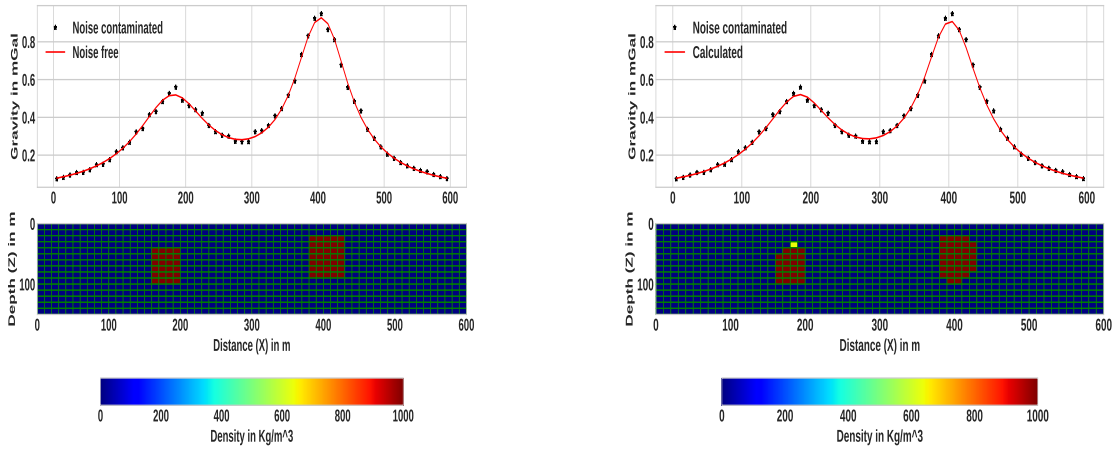
372 To evaluate the functionality and efficiency of the method, the developed procedure was tested on sev-
373 eral synthetic model examples. The examples presented here are randomly chosen to demonstrate: (I)
374 the applicability of the proposed auto-adaptive regularization technique (Eq. (18)) and error weighting
375 function (Eq. (16)); (II) the performance of the method in producing compact and sharp images of the
376 causative bodies; (III) the effectiveness of the combined stopping criterion. The forward and the inverse
377 problem were carried out using the procedure described in the preceding sections. In the inversion of the

378 synthetic examples, the same subsurface discretization as the one used in generating the synthetic data
379 (Forward modeling) is used. All the inversion tests are performed on a Desktop computer (11th Gen
380 Intel(R) Core(TM) i7-11700, 2.50GHz processor). For the first and second synthetic examples presented
381 in this work: (I) The model region was discretized into 60 x 15 rectangular cells and the dimensions of
382 each cell were taken as 10 x 10 m, in the X and Y directions respectively. (II) The synthetic gravity data
383 were computed at 60 data points that are centered in each cell at the top side of the model, to produce
384 data at 10 m sample interval. (III) The computed gravity data are contaminated with Gaussian noise
385 that has a standard deviation that amounts to 4 % of the magnitude at each data point with zero mean
386 (Farquharson, 2008; Rezaie et al., 2017).

387 The first synthetic data inversion has been done for the model presented in Fig. 3(a). For this synthetic
388 model the causative bodies are two rectangular structures elongated differently in the horizontal and
389 vertical directions and located at different depths. The causative bodies have the same density contrast
390 1000 kg/m^3 . The density of the causative bodies are given relative to the zero density of uniform back-
391 ground. Figure 3(a) upper panel shows noise free (solid line) and noise contaminated (star dots) gravity
392 data. Separate inversion runs, for three different ℓ_o values (0.2, 0.3 and 0.4), were performed with the
393 developed inversion method. Note that, for subsequent iterations the proposed auto-adaptive regular-
394 ization technique (Eq. (18)) is used to compute ℓ for each case. At the beginning of the inversion, the
395 iterations are initialized with $\rho_F = 0$ and $\mathbf{W}_h = \mathbf{W}_c = \mathbf{W}_n = \mathbf{W}_{L_0} = \mathbf{I}$. The lower limit density
396 contrasts of all cells is zero ($\rho_{min} = 0$) and the upper bound $\rho_{max} = 1000 \text{ kg/m}^3$.

397 The results of the inversion by using the developed method for three different ℓ_o values are shown in
398 Figs. 3(b) and 4. The corresponding data fit between the predicted (solid line) and the actual contam-
399 inated (stars) gravity data are also shown. Comparing the inversion results with the original synthetic
400 model in Fig. 3(a), the inversion has sufficiently recovered the true models. The depth, geometry, and
401 density distributions of the synthetic causative bodies were recovered adequately. This can confirm
402 the applicability of the proposed auto-adaptive regularization technique (Eq. (18)) and error weighting
403 function (Eq. (16)). Notice that the results also indicate the robustness and stability of the developed
404 inversion method for different ℓ_o values. The average computation time to finish the inversion is approx-
405 imately 16.3 seconds.

406 The second synthetic model is more complicated and consists of two causative bodies placed at various
407 depth. The bodies have different sizes, shapes, and density contrasts. The first causative body is a verti-
408 cal rectangular block, with density contrast 2000 kg/m^3 , placed at 40 m depth and the second body is

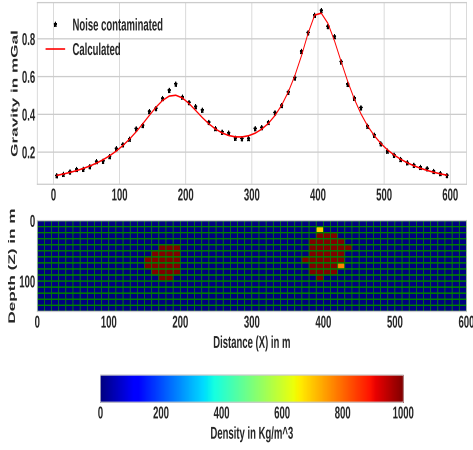


(a) The lower panel represents 2-D synthetic model, which constitutes two isolated rectangular bodies located at various depths and the top panel shows the gravity anomaly due to these two subsurface rectangular bodies.

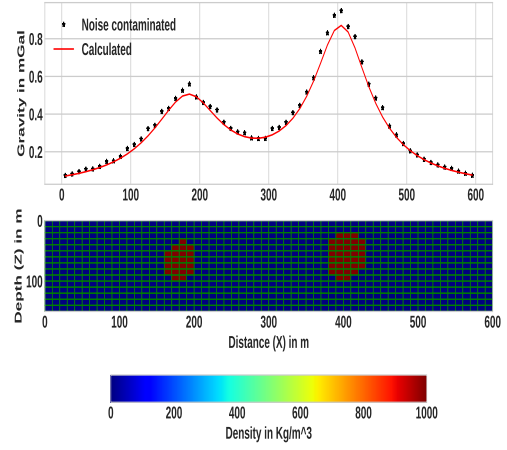
(b) The lower panel represents the subsurface, as a result of the proposed inversion method using $\ell_o = 0.3$ and the top panel shows the synthetic data together data derived from the model.

Figure 3: The first synthetic model and the result of the inversion.

409 a dipping dike with density contrast 3000 kg/m^3 at 20 m depth. The synthetic model is shown in the
 410 lower part of Fig. 5(a) and the generated noise-corrupted and noise free gravity data are shown on the
 411 upper part. Using the generated synthetic data, the inversion was initiated by assigning an initial zero
 412 density to each cell. We set initial $\ell_o = 0.3$. The density contrast limits are bounded between lower
 413 bound $\rho_{min} = 0$ and the upper bound $\rho_{max} = 3000 \text{ kg/m}^3$. Even though a maximum iteration of 20
 414 was set, the *misfit* and *smv* between two consecutive iterations gradually fall below the threshold set
 415 after the 14th iteration. The total computation time is approximately 15.73 seconds. In Fig. 5(b), the
 416 resulting model from the inversion of the second synthetic model (Fig. 5(a)) using the proposed method
 417 is presented. As can be seen in Fig. 5(b) upper panel the modeled gravity data (solid line) fits adequately
 418 with the synthetic data. The result, presented in Fig. 5(b) lower panel, indicates an acceptable recon-
 419 struction of the synthetic multi-sources and multi-shape bodies that are located at different depths. The
 420 true shape, location and density of the causative bodies are recovered adequately. Like the first example
 421 the reproduced images of the localized multiple sources are compact and sharp (Fig. 5(b) lower panel).
 422 For the third and fourth synthetic examples: (I) The subsurface model was discretized into 100 x 20
 423 rectangular cells. Each cell has a size of 50 m in X and Z directions. (II) The synthetic gravity data were
 424 computed on 100 data points with a sample spacing of 50 m. The third synthetic model includes two
 425 dipping dikes in opposite directions. The causative 2-D bodies have different sizes and the same density



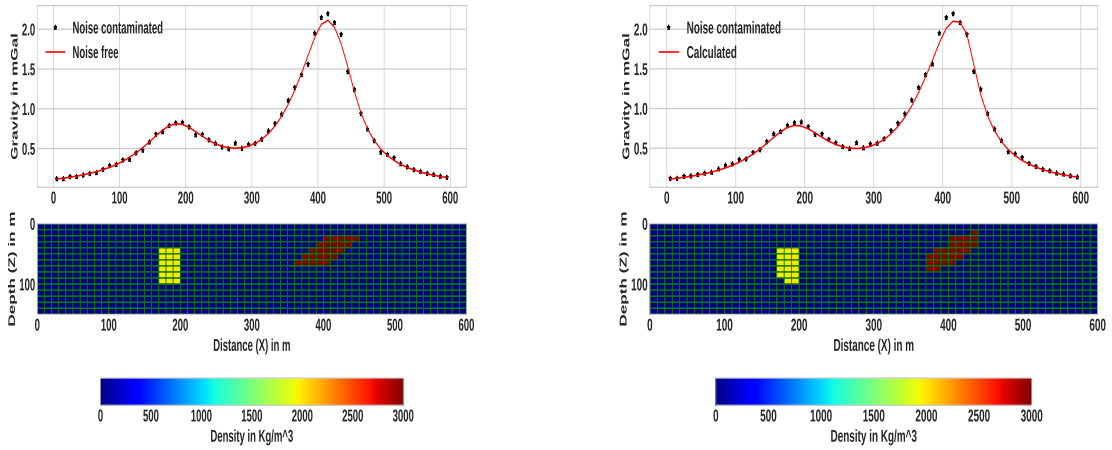
(a) Using $\ell_o = 0.2$.



(b) Using $\ell_o = 0.4$.

Figure 4: Inversion results, using different ℓ_o values, for the first synthetic model given in Fig. 3(a).

426 contrast that amounts to $1000 \text{ kg}/\text{m}^3$ in a homogeneous background zero density. The top part of the
 427 shallower dipping dike lies at a depth of 200 m and that of the deeper dike at a depth of 250 m. The
 428 computed gravity data were contaminated by uncorrelated Gaussian noise whose standard deviation was
 429 equal to 4% of the difference between the maximum and the minimum anomaly and zero mean. The
 430 synthetic model and the corresponding data are shown in Fig. 6 at lower and upper panels respectively.
 431 The inversion process was commenced by setting the densities of all cells to zero. The initial value of
 432 ℓ_o was set to 0.4. The bounding density ranges were set to a minimum value $\rho_{min} = 0$ and maximum
 433 value $\rho_{max} = 1000 \text{ kg}/\text{m}^3$. The maximum number of iterations was set to 20. Here, the inversion
 434 converged after the 13th iteration and the total computation time is approximately 66.49 seconds. The
 435 resulting model and the inverted data using the proposed method are shown in Fig. 7(b). For the sake
 436 of comparison keeping all inversion parameters the same, the synthetic data was also inverted with the
 437 classical L_2 -norm regularized inversion approach and the obtained result is shown in Fig. 7(a). As it
 438 can be seen from the lower panel of Fig. 7(b), unlike the model in Fig. 7(a), the developed method was
 439 able to produce a compact and sharp model successfully. The other concern, which can be seen from
 440 the result in Fig. 7(a), is that the target density contrast values are underestimated in the case of the
 441 conventional L_2 -norm inversion. In contrast, the geometrics, locations, and densities of both anomalous
 442 structures were adequately recovered with the presented inversion method (see Fig. 7(b)).
 443 The fourth synthetic model consists of two different rectangular anomalous bodies (Fig. 8(a) lower
 444 panel). The anomalous structures have different dimensions and are buried at different depths. The top



(a) Synthetic model consisting of a dipping dike and vertical rectangular block and the corresponding gravity data.

(b) The density model obtained by inverting the gravity data using the developed method. The predicted data as a result of inversion process are shown on the top panels (solid line).

Figure 5: The second example synthetic model and the corresponding inversion result.

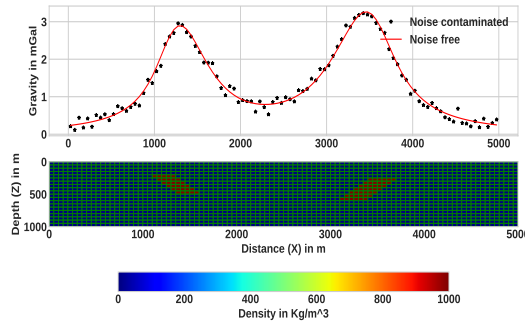
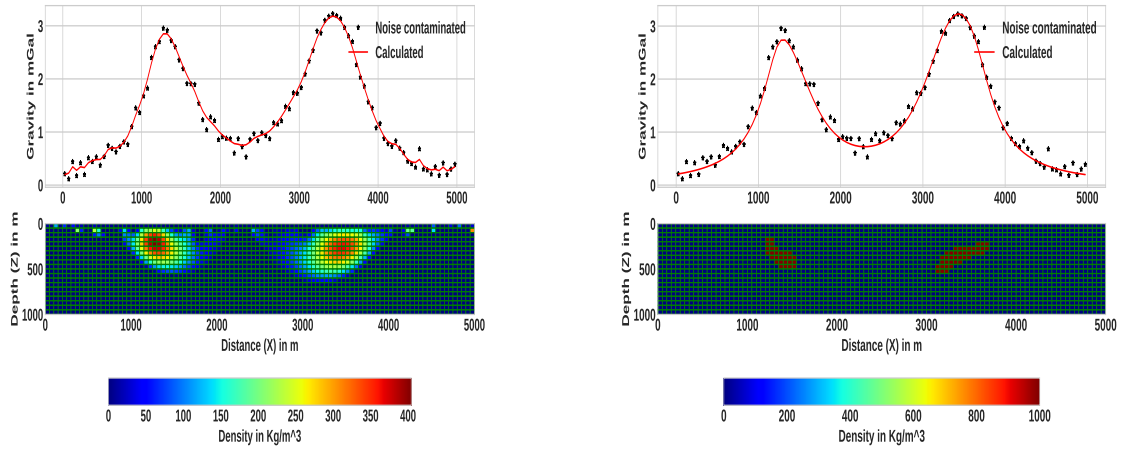


Figure 6: The third synthetic model that comprises two dikes at various depths with the density contrast that amounts to 1000 kg/m^3 and the corresponding gravity data.

445 of the first rectangular block is placed at a depth of 200 m and its density contrast is -1000 kg/m^3 while
 446 the top of the second block is placed at a depth of 250 m and has a density contrast of 1000 kg/m^3 .
 447 Different density contrast, size, and depth of adjacent structures have been considered to show the ability
 448 of the presented inversion method in reconstructing true parameters for these models. In this synthetic
 449 example, the computed data are contaminated by Gaussian noise with a standard deviation of 3% of the
 450 difference between the maximum and the minimum anomaly.

451 For the current example, the inversion process was initialized by setting the initial value of $\ell_o = 0.5$.
 452 The lower bound for the density constraint $\rho_{min} = -1000 \text{ kg/m}^3$ and the upper bound $\rho_{min} = 1000$
 453 kg/m^3 . Similar to the previous examples, though the maximum number of iterations was set to be 20,



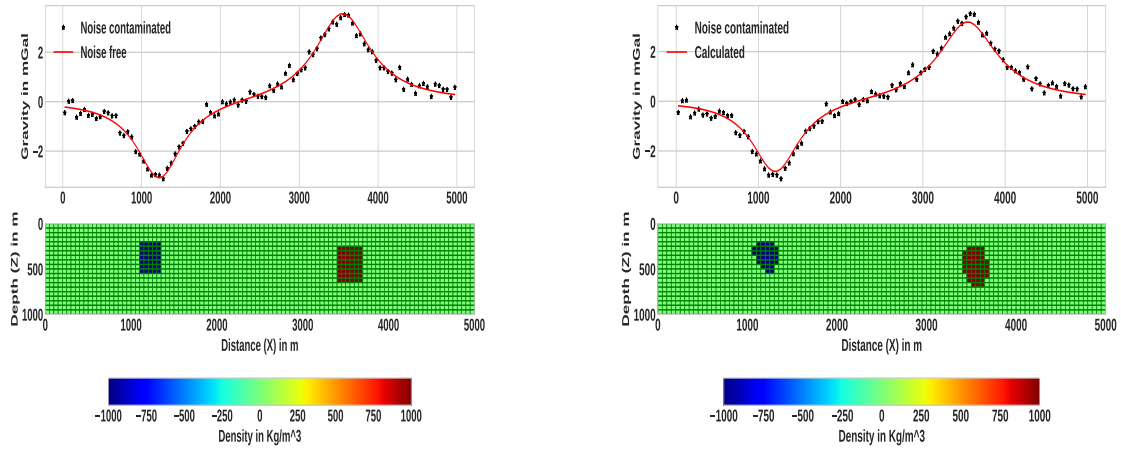
(a) Using the conventional minimum norm (L_2 -norm) smooth stabilizer and the corresponding data fit.

(b) Using the presented method

Figure 7: Inversion results of the third synthetic example in Fig. 6.

454 the iterative step terminated when the proposed combined criterion is satisfied after 11 iterations. The ap-
455 proximate running time required to finish the inversion is 55.64 seconds. Figure 8(b) lower panel shows
456 the recovered density contrast model. The corresponding fits between synthetic (stars) and predicted
457 data (line) are shown in the upper panel of the same figure. We can see that the recovered rectangular
458 bodies are compact and have sharp boundaries. The obtained results also indicate that the depth and
459 density contrast of the anomalous rectangular bodies have been determined sufficiently.

460 Here, the effectiveness and the advantage of the proposed combined stopping criterion are illustrated
461 by comparing it with another commonly used stopping condition. For this reason, the inversion process
462 was performed again with the developed inversion method using only the misfit function ($|misfit^{k-1} -$
463 $misfit^k|$) as a stopping condition. Note that, for comparison purposes, all the other inversion parame-
464 ters are set the same except for the stopping criterion. The resulting recovered density contrast models
465 and the data fit are presented in Fig. 9. The corresponding values of the $misfit$ and smv as a function
466 of iteration number are also shown in Fig. 10(a). For the sake of comparison, the $misfit$ and smv
467 when using the proposed combined stopping criterion for the same data set are also presented in Fig.
468 10(b). The stopping condition $|misfit^{k-1} - misfit^k| \leq \mu$ was reached after 5 iterations, as shown
469 in the curve of Fig. 10(a) before the true density distribution has been recovered fully. In other words,
470 the estimated models are not satisfactory because densities lower than the target density are observed
471 around the edges of the anomalous bodies (Fig. 9). This indicates that unlike the result presented in
472 Fig. 8(b), where the proposed combined stopping condition is used, quitting the iterative process only



(a) Synthetic model consisting of two rectangular bodies at various depths with different density contrast and the corresponding noise free and contaminated gravity anomalies.

(b) The lower panel shows recovered density contrast model obtained by inverting the gravity data using the developed method, while the upper one shows the associated fits between the synthetic data that is taken from (a) and the predicted response.

Figure 8: The fourth synthetic model example and the corresponding inversion result.

473 with $|misfit^{k-1} - misfit^k| \leq \mu$ criterion produces a premature solution that is before the maximum
 474 compactness is achieved.

A number of other numerical experiments we carried out showed that there are situation where either

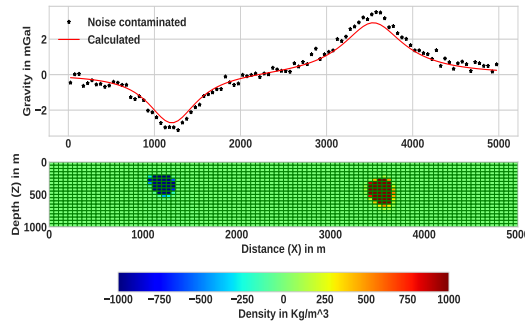
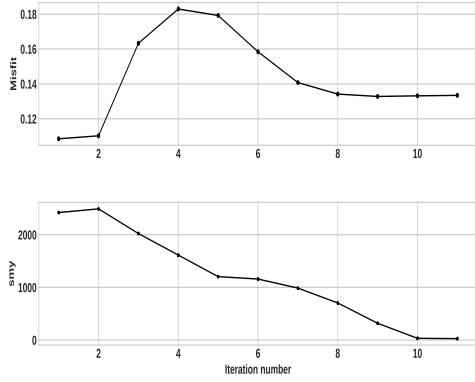
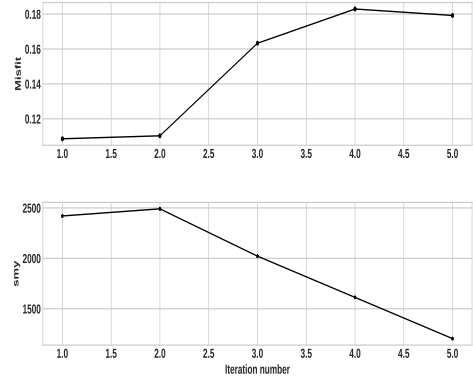


Figure 9: Inversion result obtained using only the commonly used criterion ($|misfit^{k-1} - misfit^k|$) and the corresponding data fit (upper panels) for the synthetic example in Fig. 8(a). The obtained density model shows that compact and sharp model is not approximately achieved due to the termination before the iterative procedure has reached convergence.

475
 476 $|misfit^k|$ or $|misfit^{k-1} - misfit^k|$ fall below the given threshold values, at earlier iterations, before the
 477 true density is fully recovered. Thus, it is hard to take only one criterion as a termination condition. As
 478 stated in Sect. 2.3.6, it has been mentioned that the same has also be pointed out in number of previous
 479 works (Rao et al., 2018). Whereas, in the case of the proposed criterion that is when both the conditions



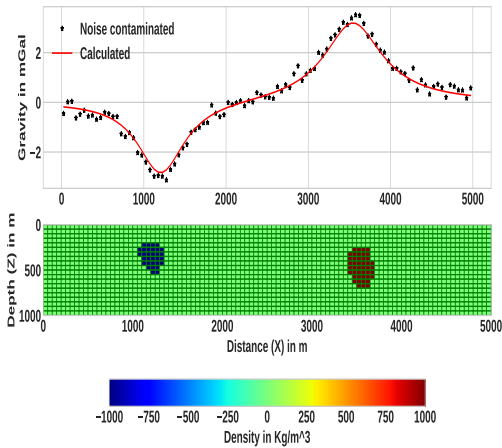
(a) Using the proposed combined stopping condition



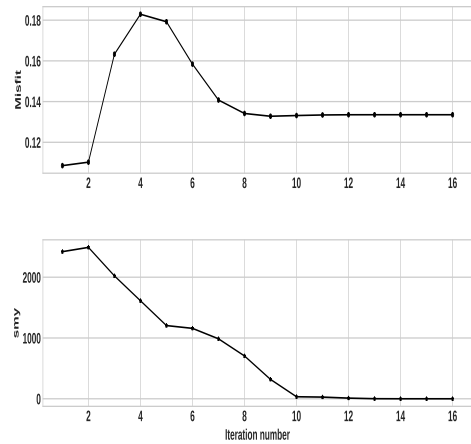
(b) Using only $|misfit^{k-1} - misfit^k| \leq \mu$

Figure 10: The progression of $misfit$ and sm_y in the course of the iteration during the inversion of the fourth example synthetic data.

480 $|sm_y^{k-1} - sm_y^k| \leq \tau$ and $|misfit^{k-1} - misfit^k| \leq \mu$ are satisfied at the same time the inversion
 481 process yields an acceptable model. This clearly illustrates the advantage of using the proposed stopping
 criterion and its effectiveness in quitting the iterative scheme after optimal number of iterations. To fur-



(a) The obtained recovered density model (lower panel) and the corresponding data fit (upper panel).



(b) Progression of $misfit$ (top panel) and sm_y (lower panel) in the course of the iterative procedure.

Figure 11: Late iteration termination (at 16th iteration) inversion result and the corresponding $misfit$ and sm_y variation with iteration number for the fourth example in Fig 8.

482

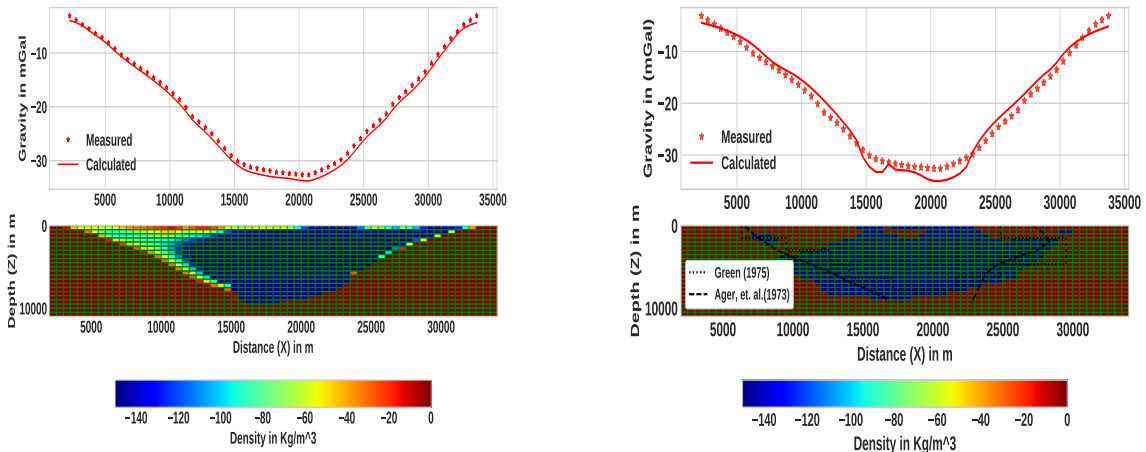
483 ther illustrate the effectiveness of the proposed combined criterion, the inversion process is allowed to
 484 continue to the 16th iteration and the model as a result of this is presented in Fig. 11(a). The progression
 485 of the $misfit$ and sm_y in the course of the iterative procedure are also given in Fig. 11(b). As it can be
 486 seen from the result (Fig. 11(b)) the solution obtained at subsequent iterations, after the 11th iteration

487 where the iteration is terminated with the proposed stopping condition, remains virtually unaltered. This
488 can also be observed from the *misfit* and *smv* variation curves shown in Fig. 11(b), in such that after
489 11th iteration the *misfit* and *smv* values remain literally unchanged. Moreover, the results also indicate
490 the appropriateness of the suggested threshold values μ and τ used in the proposed stopping criterion.
491 The other thing one can observe from the results in Fig. 11 is the stability of the developed inversion
492 method. This can also illustrate the effectiveness of the newly proposed auto-adaptive regularization
493 technique (Eq. (18)) and error weighting function (Eq. (16)).

494 In general, the presented method was tested with noise contaminated data that are generated from dif-
495 ferent geometries, locations, sizes, and densities contrasts of causative bodies and it has successfully
496 recovered all models. Moreover, all the reconstructed images of the presented synthetic models are
497 compact and sharp. Numerous synthetic data inversions were performed to analyze the impact of the
498 density contrast bounds. The obtained results, which are not presented here, suggest that the values of
499 density contrast bounds have a significant effect on the results, and hence to recover a feasible model a
500 good knowledge of the density bounds is vital. This also pointed out by number of authors, for exam-
501 ple Vatankhah et al. (2017); Li et al. (2018) and Utsugi (2019), in the case of inversion methods that
502 use non-smooth stabilizers (L_1 -norm or L_0 -norm). Provided that the lower and upper density contrast
503 bounds are chosen properly, this inversion technique produces acceptable solutions. Therefore, as it was
504 demonstrated using synthetic examples, the proposed method has effectively and efficiently recovered
505 the synthetic models. Generally, the tests performed on different geometry synthetic models showed that
506 the method gives acceptable results for localized multi-sources anomalies at different depths with sharp
507 features.

508 **4 Real Data Test**

509 To test the method in the real world, where the gravity data is contaminated with noise the improved
510 algorithm is implemented on gravity data acquired on different published geologic settings. The first one
511 is taken from Green (1975) by carefully digitizing the residual gravity data. As it was given in Green
512 (1975) the data was measured over the Guichon Creek batholith in south-central British Columbia. For
513 the details about the measurement and geology the reader is referred to Ager et al. (1973) and Ager
514 (1972). The residual gravity profile is digitized at a regular intervals of 0.5 km to produce a total of 64
515 data points as shown in Fig. 12 (star marks).



(a) Using the conventional minimum norm (L_2 -norm) smooth stabilizer.

(b) Using the presented method

Figure 12: The observed gravity anomaly over Guichon Creek batholith in south-central British Columbia (after Green (1975)) and its inversion results. Digitized data (star marks) with calculated data (solid line) are shown on the top panels of each subfigure. The corresponding recovered density contrast models are shown on the bottom. For comparison, the results obtained by Ager et al. (1973), which was obtained from drilling and Green (1975) are also presented.

516 For the inversion, the source volume beneath the anomaly was divided into 64×22 square lattice with
 517 dimensions of each cell being 0.5 km in both X and Z-directions. Based on the a prior information from
 518 Ager (1972) density values were constrained between the limits $\rho_{min} = -150 \text{ kg/m}^3$ and $\rho_{max} = 0.001$
 519 kg/m^3 . We start the inversion with a homogeneous initial model in which every block has the same
 520 zero density and an initial ℓ_o value of 0.48. The inversion was terminated after 9th iteration because the
 521 stopping criteria are fulfilled. The resulting model is presented in Fig. 12(b). For comparison, the results
 522 obtained by Ager et al. (1973) and Green (1975) are also included in Fig. 12(b). In addition, using the
 523 same inversion parameters we have performed L_2 -norm regularized inversion and the obtained result is
 524 shown in Fig. 12(a). The shape, real extent of the anomaly, and depth to bottom from the developed
 525 method are very close to the true geological feature (Ager et al., 1973) which was obtained from drilling.
 526 That means the implementation of the presented method resulted in a better solution compared to Green
 527 (1975) and the conventional L_2 -norm inversion. Note that, this reasonable result is obtained by using
 528 only the density contrast limits as a prior information.

529 The second test on measured gravity data is carried out using the published data by Last and Kubik
 530 (1983) over the Woodlawn massive sulfide ore body, New South Wales, Australia. The residual anomaly
 531 of the area consisting of 61 data measurements, sampled every 5 m, is digitized from Last and Kubik

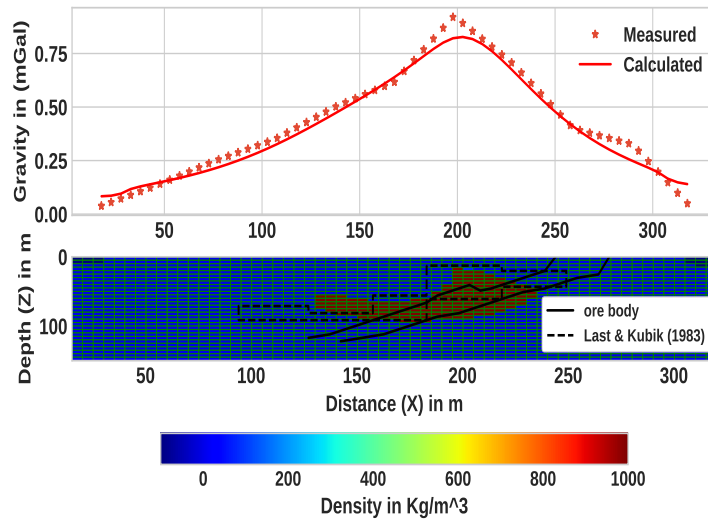


Figure 13: An observed gravity anomaly over the Woodlawn ore body, New South Wales (After Last and Kubik (1983)) and the its inversion result. The digitized data (star marks) is shown together with calculated data (solid line) on the top panel. The corresponding recovered density contrast model after 11th iteration shown on bottom panel and the ore body proved by drilling is shown with solid line. The recovered body density contrast is represented by the color scale bar.

532 (1983). The details about the data measurement and the geology of the area are discussed in Whiteley
 533 (1981). The model subsurface was divided into 61 by 30 blocks with a dimension of 5 m in both X-
 534 and Z-direction. Inverse modeling was performed with bounding constraints $\rho_{min} = -600$ and ρ_{max}
 535 $= 1000 \text{ kg/m}^3$. The initial given value for ℓ_o is 0.6. The final solution was obtained after the 11th
 536 iteration. The reconstructed model including the final model of Last and Kubik (1983) are shown in
 537 Fig. 13. The cross-section of the ore body verified by drilling (Whiteley, 1981) is also shown in the
 538 figure. The recovered model is approximately coincident with the shape, depth of burial and density of
 539 the known ore body. Areas of misfits in the current and previous works are believed to be caused by the
 540 termination of the original data at both ends before it reaches the background level. Thus, this can be
 541 additional evidence that the presented method can be successfully applied to real data.

542 5 Conclusion

543 We have presented an alternative gravity inversion method that can produce compact and sharp images
 544 by using the L_0 -norm stabilizing functional that helps to model geological features with non-smooth,
 545 blocky geologic bodies. Physical parameter inequality constraints, and depth weighting are integrated

546 into the procedure. The method also incorporates an auto-adaptive regularization technique, which auto-
547 matically determines a suitable regularization parameter at every iteration, and an error weighting func-
548 tion that helps to improve both the stability and convergence of the method. One of the strongest sides of
549 the proposed auto-adaptive regularization and error weighting matrix is that they are not dependent on a
550 priori knowledge of the noise level. Because of that, the method can yield reasonable results even when
551 the noise level of the data is not known properly. We implemented a combined stopping criteria and
552 illustrated its effectiveness to terminate the iterative inversion process after an optimal number of steps.
553 To illustrate the efficiency and the capacity of the proposed procedure numerous synthetic tests were
554 done. From these, four synthetic examples were presented. According to the results from these syn-
555 thetic examples, the method can be applied for multi-source localized bodies located at different depths
556 and having different geometries with sharp features. Furthermore, the method proved to be efficient in
557 resolving causative bodies both vertically and laterally and produced compact and sharp images. The
558 obtained results also indicate that the method behaves well with different noise levels embedded in the
559 data and still retains its stability. This can confirm the robustness and stability of the developed inversion
560 method for different noise levels. The method was also tested on measured gravity data. We obtained
561 geologically acceptable models and the results showed that our approach is effective and reliable. From
562 a computational point of view, the method is efficient and can be easily run on a personal computer just
563 in a few seconds. In conclusion, the developed method is advantageous in such that it is stable, efficient,
564 and resolves sharp subsurface features with acceptable resolving capacity. In geophysical exploration
565 gravity data are more often used to image complex 3D structures of the subsurface, hence further de-
566 velopment of the method to 3D is crucial. Accordingly, future work will deal with the extension of the
567 presented method to 3D gravity inversion algorithm.

568 **Data Availability**

569 The authors confirm that the real data supporting the findings of this study are available within the
570 articles:

- 571 1. Green, W. R. (1975) Inversion of gravity profiles by use of a backus-gilbert approach. *Geophysics*,
572 40, 763–772 . and its supplementary material.
- 573 2. Last, B. and Kubik, K. (1983) Compact gravity inversion. *Geophysics*, 48, 713–721. and its
574 supplementary material

575 **Author contributions**

576 MGG developed the methodology; EL supervised the research work; MGG wrote the manuscript draft;
577 EL reviewed and edited the manuscript.

578 **Competing interests**

579 The authors declare that they have no known competing financial interests or personal relationships that
580 could have appeared to influence the work reported in this paper.

581 **Acknowledgements**

582 This work was sponsored by Wolkite and Addis Ababa Universities. We are thank full to all members
583 of the Institute of Geophysics, Space Science and Astronomy of Addis Ababa University for all their
584 assistance and allowing to use different office and computational facilities. Most importantly we thank
585 Filagot Mengistu for her limitless support to this research work. The authors are grateful to the editor's
586 and reviewers' constructive comments and corrections on the improvement of this paper. The authors
587 also would like to thank Prof. Tilahun Mammo and Prof. André Kazuo for their careful reading and
588 comments during the work.

References

- 589
590 Ager, C., Ulrych, T., and McMillan, W.: A gravity model for the Guichon Creek batholith, south-central
591 British Columbia, *Canadian Journal of Earth Sciences*, 10, 920–935, 1973.
- 592 Ager, C. A.: A gravity model for the Guichon Creek Batholith, Ph.D. thesis, University of British
593 Columbia, 1972.
- 594 Ajo-Franklin, J., Minsley, B., and Daley, T.: Applying compactness constraints to differential traveltome
595 tomography: *Geophysics*, 72, R67–R75, 2007.
- 596 Al-Chalabi, M.: Some studies relating to nonuniqueness in gravity and magnetic inverse problems,
597 *Geophysics*, 36, 835–855, 1971.
- 598 Aster, R. C., Borchers, B., and Thurber, C. H.: *Parameter estimation and inverse problems*, Elsevier,
599 2018.
- 600 Barbosa, V. C. F. and Silva, J. B.: Generalized compact gravity inversion, *Geophysics*, 59, 57–68, 1994.
- 601 Bertete-Aguirre, H., Cherkaev, E., and Oristaglio, M.: Non-smooth gravity problem with total variation
602 penalization functional, *Geophysical Journal International*, 149, 499–507, 2002.
- 603 Blakely, R. J.: *Potential theory in gravity and magnetic applications*, Cambridge university press, 1996.
- 604 Borges, L. S., Bazán, F. S. V., and Cunha, M. C.: Automatic stopping rule for iterative methods in
605 discrete ill-posed problems, *Computational and Applied Mathematics*, 34, 1175–1197, 2015.
- 606 Boulanger, O. and Chouteau, M.: Constraints in 3D gravity inversion, *Geophysical prospecting*, 49,
607 265–280, 2001.
- 608 Camacho, A. G., Montesinos, F. G., and Vieira, R.: A 3-D gravity inversion tool based on exploration
609 of model possibilities, *Computers & Geosciences*, 28, 191–204, 2002.
- 610 Camacho, A. G., Fernández, J., and Gottsmann, J.: A new gravity inversion method for multiple sub-
611 horizontal discontinuity interfaces and shallow basins, *Journal of Geophysical Research: Solid Earth*,
612 116, 2011.
- 613 Cella, F. and Fedi, M.: Inversion of potential field data using the structural index as weighting function
614 rate decay, *Geophysical Prospecting*, 60, 313–336, 2012.

615 Commer, M.: Three-dimensional gravity modelling and focusing inversion using rectangular meshes,
616 *Geophysical Prospecting*, 59, 966–979, 2011.

617 Ekinci, Y. L.: 2D focusing inversion of gravity data with the use of parameter variation as a stopping
618 criterion, *Journal of the Balkan geophysical society*, 11, 1–9, 2008.

619 Farquharson, C. G.: Constructing piecewise-constant models in multidimensional minimum-structure
620 inversions, *Geophysics*, 73, K1–K9, 2008.

621 Farquharson, C. G. and Oldenburg, D. W.: A comparison of automatic techniques for estimating the
622 regularization parameter in non-linear inverse problems, *Geophysical Journal International*, 156, 411–
623 425, 2004.

624 Fei, Z., Chunhui, T., Tao, W., Zhaofa, Z., and Cai, L.: 3D focused inversion of near-bottom magnetic
625 data from autonomous underwater vehicle in rough seas, *Ocean Science Journal*, 53, 405–412, 2018.

626 Feng, X., Liu, S., Guo, R., Wang, P., and Zhang, J.: Gravity inversion of blocky basement relief using
627 L_0 -norm constraint with exponential density contrast variation, *Pure and Applied Geophysics*, 177,
628 3913–3927, 2020.

629 Fournier, D., Heagy, L. J., and Oldenburg, D. W.: Sparse magnetic vector inversion in spherical coordi-
630 nates Sparse magnetic vector inversion, *Geophysics*, 85, J33–J49, 2020.

631 Gebre, M. G. and Lewi, E.: L_0 -norm gravity inversion with new depth weighting function and bound
632 constraints, *Acta Geophysica*, 70, 1619–1634, 2022.

633 Ghalehnoee, M. H., Ansari, A., and Ghorbani, A.: Improving compact gravity inversion based on new
634 weighting functions, *Geophysical Journal International*, 208, 546–560, 2017.

635 Gholami, A. and Aghamiry, H. S.: Iteratively re-weighted and refined least squares algorithm for robust
636 inversion of geophysical data, *Geophysical Prospecting*, 65, 201–215, 2017.

637 Grandis, H. and Dahrin, D.: Constrained two-dimensional inversion of gravity data, *Journal of Mathe-
638 matical and Fundamental Sciences*, 46, 1–13, 2014.

639 Green, W. R.: Inversion of gravity profiles by use of a Backus-Gilbert approach, *Geophysics*, 40, 763–
640 772, 1975.

- 641 Guillen, A. and Menichetti, V.: Gravity and magnetic inversion with minimization of a specific func-
642 tional, *Geophysics*, 49, 1354–1360, 1984.
- 643 Hinze, W. J., Von Frese, R. R., Von Frese, R., and Saad, A. H.: Gravity and magnetic exploration:
644 principles, practices, and applications, Cambridge University Press, 2013.
- 645 Last, B. and Kubik, K.: Compact gravity inversion, *Geophysics*, 48, 713–721, 1983.
- 646 Lelièvre, P. G., Oldenburg, D. W., and Williams, N. C.: Integrating geological and geophysical data
647 through advanced constrained inversions, *Exploration Geophysics*, 40, 334–341, 2009.
- 648 Lelievre, P. G., Farquharson, C. G., and Bijani, R.: 3D potential field inversion for wireframe surface
649 geometry, in: 2015 SEG Annual Meeting, OnePetro, 2015.
- 650 Levin, E. and Meltzer, A. Y.: Stopping criterion for iterative regularization of large-scale ill-posed prob-
651 lems using the Picard parameter, arXiv preprint arXiv:1707.04200, 2017.
- 652 Lewi, E.: Modelling and inversion of high precision gravity data, Ph.D. thesis, Verlag der Bayerischen
653 Akademie der Wissenschaften, Munchen, Germany, ISSN 0065 -5325, ISBN3769695119., 1997.
- 654 Li, F., Xie, R., Song, W., Zhao, T., and Marfurt, K.: Optimal L_q -norm regularization for sparse re-
655 flectivity inversion, in: SEG Technical Program Expanded Abstracts 2017, pp. 677–681, Society of
656 Exploration Geophysicists, 2017.
- 657 Li, Y. and Oldenburg, D. W.: 3-D inversion of magnetic data, *Geophysics*, 61, 394–408, 1996.
- 658 Li, Y. and Oldenburg, D. W.: 3-D inversion of gravity data, *Geophysics*, 63, 109–119, 1998.
- 659 Li, Y. and Oldenburg, D. W.: Fast inversion of large-scale magnetic data using wavelet transforms and a
660 logarithmic barrier method, *Geophysical Journal International*, 152, 251–265, 2003.
- 661 Li, Z. and Yao, C.: 3D sparse inversion of magnetic amplitude data when strong remanence exists, *Acta*
662 *Geophysica*, pp. 1–11, 2020.
- 663 Li, Z., Yao, C., Zheng, Y., Wang, J., and Zhang, Y.: 3D magnetic sparse inversion using an interior-point
664 method, *Geophysics*, 83, J15–J32, 2018.
- 665 Meng, Z.: 3D inversion of full gravity gradient tensor data using SL0 sparse recovery, *Journal of Applied*
666 *Geophysics*, 127, 112–128, 2016.

- 667 Meng, Z.-H., Xu, X.-C., and Huang, D.-N.: Three-dimensional gravity inversion based on sparse recovery iteration using approximate zero norm, *Applied Geophysics*, 15, 524–535, 2018.
- 668
- 669 Menke, W.: *Geophysical data analysis: Discrete inverse theory*, International Geophysics Series, New York: Academic Press, 1989.
- 670
- 671 Nagy, D.: The gravitational attraction of a right rectangular prism, *Geophysics*, 31, 362–371, 1966.
- 672 Paoletti, V., Ialongo, S., Florio, G., Fedi, M., and Cella, F.: Self-constrained inversion of potential fields, *Geophysical Journal International*, 195, 854–869, 2013.
- 673
- 674 Peng, G. and Liu, Z.: 3D inversion of gravity data using reformulated L_p -norm model regularization, *Journal of Applied Geophysics*, 191, 104–117, 2021.
- 675
- 676 Pilkington, M.: 3D magnetic data-space inversion with sparseness constraints, *Geophysics*, 74, L7–L15, 2008.
- 677
- 678 Portniaguine, O. and Zhdanov, M. S.: Focusing geophysical inversion images, *Geophysics*, 64, 874–887, 1999.
- 679
- 680 Rao, K., Malan, P., and Perot, J. B.: A stopping criterion for the iterative solution of partial differential equations, *Journal of Computational Physics*, 352, 265–284, 2018.
- 681
- 682 Rezaie, M. and Moazam, S.: A new method for 3-D magnetic data inversion with physical bound, *Journal of Mining and Environment*, 8, 501–510, 2017.
- 683
- 684 Rezaie, M., Moradzadeh, A., Kalate, A. N., and Aghajani, H.: Fast 3D focusing inversion of gravity data using reweighted regularized Lanczos bidiagonalization method, *Pure and Applied Geophysics*, 174, 359–374, 2017.
- 685
- 686
- 687 Silva, J. B. and Barbosa, V. C.: Interactive Gravity Inversion, *Geophysics*, 71, J1–J9, 2006.
- 688
- 689 Silva, J. B., Medeiros, W. E., and Barbosa, V. C.: Potential-field inversion: Choosing the appropriate technique to solve a geologic problem, *Geophysics*, 66, 511–520, 2001.
- 690
- 691 Singh, A., Sharma, S. P., Akca, İ., and Baranwal, V. C.: Fuzzy constrained L_p -norm inversion of direct current resistivity data, *Geophysics*, 83, E11–E24, 2018.

- 692 Stocco, S., Godio, A., and Sambuelli, L.: Modelling and compact inversion of magnetic data: A Matlab
693 code, *Computers & Geosciences*, 35, 2111–2118, 2009.
- 694 Sun, J. and Li, Y.: Adaptive L_p inversion for simultaneous recovery of both blocky and smooth features
695 in a geophysical model, *Geophysical Journal International*, 197, 882–899, 2014.
- 696 Tikhonov, A. N., Goncharsky, A., Stepanov, V., and Yagola, A. G.: Numerical methods for the solution
697 of ill-posed problems, vol. 328, Springer Science & Business Media, 2013.
- 698 Utsugi, M.: 3-D inversion of magnetic data based on the L_1 - L_2 -norm regularization, *Earth, Planets and*
699 *Space*, 71, 1–19, 2019.
- 700 Varfinezhad, R., Oskooi, B., and Fedi, M.: Joint inversion of DC resistivity and magnetic data, con-
701 strained by cross gradients, compactness and depth weighting, *Pure and Applied Geophysics*, 177,
702 4325–4343, 2020.
- 703 Varfinezhad, R., Fedi, M., and Milano, M.: The role of model weighting functions in the gravity and DC
704 resistivity inversion, *IEEE Transactions on Geoscience and Remote Sensing*, 60, 1–15, 2022.
- 705 Vatankhah, S., Ardestani, V. E., and Renaut, R. A.: Automatic estimation of the regularization param-
706 eter in 2D focusing gravity inversion: application of the method to the Safo manganese mine in the
707 northwest of Iran, *Journal of Geophysics and Engineering*, 11, 045 001, 2014.
- 708 Vatankhah, S., Renaut, R. A., and Ardestani, V. E.: 3-D Projected L_1 inversion of gravity data using trun-
709 cated unbiased predictive risk estimator for regularization parameter estimation, *Geophysical Journal*
710 *International*, 210, 1872–1887, 2017.
- 711 Virtanen, P., Gommers, R., Oliphant, T. E., Haberland, M., Reddy, T., Cournapeau, D., Burovski, E.,
712 Peterson, P., Weckesser, W., Bright, J., et al.: SciPy 1.0: fundamental algorithms for scientific com-
713 puting in Python, *Nature methods*, 17, 261–272, 2020.
- 714 Vogel, C. R.: Computational methods for inverse problems, vol. 23, Siam, 2002.
- 715 Wang, Y. and Ma, S.: Projected Barzilai-Borwein method for large-scale nonnegative image restoration,
716 *Inverse Problems in Science and Engineering*, 15, 559–583, 2007.
- 717 Whiteley, R. J.: Geophysical Case Study of the Woodlawn Orebody, New South Wales, Australia: The
718 First Publication of Methods and Techniques Tested Over a Base Metal Orebody of the Type which

- 719 Yields the Highest Rate of Return on Mining Investment with Modest Capital Requirements. Maps,
720 Pergamon, 1981.
- 721 Zhao, C., Yu, P., and Zhang, L.: A new stabilizing functional to enhance the sharp boundary in potential
722 field regularized inversion, *Journal of Applied Geophysics*, 135, 356–366, 2016.
- 723 Zhdanov, M. and Tolstaya, E.: Minimum support nonlinear parametrization in the solution of a 3D
724 magnetotelluric inverse problem, *Inverse problems*, 20, 937, 2004.
- 725 Zhdanov, M. S.: *Geophysical inverse theory and regularization problems*, vol. 36, Elsevier, 2002.
- 726 Zhdanov, M. S.: New advances in regularized inversion of gravity and electromagnetic data, *Geophysical*
727 *Prospecting*, 57, 463–478, 2009.

728 **Figure Captions**

729 Figure 1. A 2-D model of the subsurface under a gravity profile. Gravity stations (X_i) are located
730 at the centers of the blocks, indicated by the ∇ symbols.

731 Figure 2. Comparison of the minimum support stabilizing function for different values of ε .

732 Figure 3. The first synthetic model and the result of the inversion.

733 Figure 4. Inversion results, using different ℓ_o values, for the first synthetic model given in Fig.
734 3(a).

735 Figure 5. The second example synthetic model and the corresponding inversion result.

736 Figure 6. The third synthetic model that comprises two dikes at various depths with the density
737 contrast that amounts to 1000 kg/m^3 and the corresponding gravity data

738 Figure 7. Inversion results of the third synthetic example in Fig. 6.

739 Figure 8. The fourth synthetic model example and the corresponding inversion result.

740 Figure 9. Inversion result obtained using only the commonly used criterion ($|misfit^{k-1} -$
741 $misfit^k|$) and the corresponding data fit (upper panels) for the synthetic example in Fig. 8(a).
742 The obtained density model shows that compact and sharp model is not approximately achieved
743 due to the termination before the iterative procedure has reached convergence.

744 Figure 10. The progression of $misfit$ and smv in the course of the iteration during the inversion
745 of the fourth example synthetic data.

746 Figure 11. Late iteration termination (at 16th iteration) inversion result and the corresponding
747 $misfit$ and smv variation with iteration number for the fourth example in Fig. 8(a).

748 Figure 12. The observed gravity anomaly over Guichon Creek batholith in south-central British
749 Columbia (after Green 1975) and its inversion result. Digitized data (star marks) with calculated
750 data (solid line) shown on the top panel. Corresponding recovered density contrast model after
751 9th iteration shown on the bottom panel. The recovered body density contrast is represented by
752 the color scale bar. For comparison, the results obtained by Ager (1973), which was obtained
753 from drilling and Green (1975) are also presented.

754 Figure 13. An observed gravity anomaly over the Woodlawn ore body, New South Wales (After
755 Last and Kubik (1983)) and the its inversion result. The digitized data (star marks) is shown
756 together with calculated data (solid line) on the top panel. The corresponding recovered density
757 contrast model after 11th iteration shown on bottom panel and the ore body proved by drilling is
758 shown with solid line. The recovered body density contrast is represented by the color scale bar